Chapter III

Size Dependence of Structural Characteristics in CdSe Nanocrystals

***Overview of the chapter*:**

The structural characteristics of organically passivated CdSe nanocrystals were investigated with X-ray diffraction and extended X-ray absorption fine structure. With reducing the nanocrystal size, we find that the nanocrystals with higher wurtzite stacking fraction gradually transform into a predominant zinc-blende nanocrystals via stacking faults, which can be elucidated by a thermodynamic model, and, subsequently, the changes of lattice parameters reveal an expansion in c and a contraction in a. In addition, a detail investigation on bond characteristics exhibit that, for an atomic tetrahedron, an expansion in the axial bond length $R^{(1)}$ and a contraction in the equatorial bond length $R^{(2)}$ as the particle size decreases, which have a similar behavior of distortion for the lattice parameters of the wurtzite structure. Extended X-ray absorption fine structure studies shows that the nanocrystal surface are bonding to TOPO and/or HDA molecules via Cd atoms, while the surface Se atoms remain unpassivated. We suggest that the observed hexagonal distortion is attributed to the surface stress of the nanocrystals related to the organic passivation effect and the relaxation of

atomic positions at the stacking fault interface.

3.1 Introduction

XRD and EXAFS are established as powerful techniques for determining the crystalline structure of materials. Until today, these methods are also frequently used for NCs [1-5]. In contrast with some local probes such as transmission electron microscopy or atomic-force microscopy which can probe single NC, XRD and EXAFS sample a large number of NCs to provide an average information on the internal structure. By way of analyzing XRD data, one can easily obtain the crystalline structure, lattice parameters, and domain size; EXAFS is a local structural probe which allows determining the chemical environment of a particular element. With progress in the preparation method, NCs can possess controlled quality with a narrow size distribution. We can therefore investigate the size-dependent properties of these materials using large-area probs.

The structural characteristics of NCs have a strong dependence on their size, revealing a transition behavior between solid-state physics and cluster physics. By simulating powder XRD patterns, Murray *et al.* suggested that there is a lattice contraction of 2% in CdSe NCs of ~20-Å size. Subsequently, some reports presented that the size-dependent reduction in lattice parameters of NCs is owing to the surface tension resulted from the considerable surface to interior atoms ratio [4-6]. Furthermore, it is found that the surface tension was referred to the influence of surface modification (relaxation and/or reconstruction) in which the surfactants with strong bonding would induce the surface atoms

outward while the weak NC-ligands interaction could make particle as a perfect sphere [5,7].

Atomic relaxation in wurtzite compounds was predicted using the valence force field approach by A. Marbeuf *et al*. [8]; their calculation resulted in a distorted tetrahedral structure of an extension in axial bond length $R^{(1)}$ and a contraction in equatorial bond length $R^{(2)}$. Until now, however, there is a lack of related experimental study applied in the systems of fine crystallites. The purpose in this study is to extract the distinct structural parameters of CdSe NCs by combining the results from XRD and low-temperature EXAFS analyses so that the influence of surface effects and defects on NC structure can be quantitatively explored.

3.2 Simulation of X-ray diffraction patterns

A typical powder XRD pattern from CdSe NCs taken with an X-ray photon energy of 8 keV, are plotted in Fig. 3.1 for a sample with mean diameter of 31 Å. For comparision, the diffraction of bulk CdSe which has a WZ structure is also shown. The diffraction of CdSe NCs clearly exhibits a predominantly WZ crystal structure except broader diffraction peaks. The width of a diffraction peak is inversely proportional to the number of unit cells or the coherent domain size. The observed diffraction features is due primarily to the diminished size of NC domains [9]. Some structural features such as defects can also influence the profile of the diffraction pattern [10,11]. Excessive attenuation and broadening in the (102) and (103) reflections are characteristic of stacking faults along the (002) axis [9,10]. The experimental diffraction profile is a convolution of peaks

resulting from the combination of finite size and defect broadening. Direct interpretation of peak positions and peak widths are thus unreliable measures of lattice spacing and crystallite size. Instead, modeling of the entire direction profile is performed in our study.

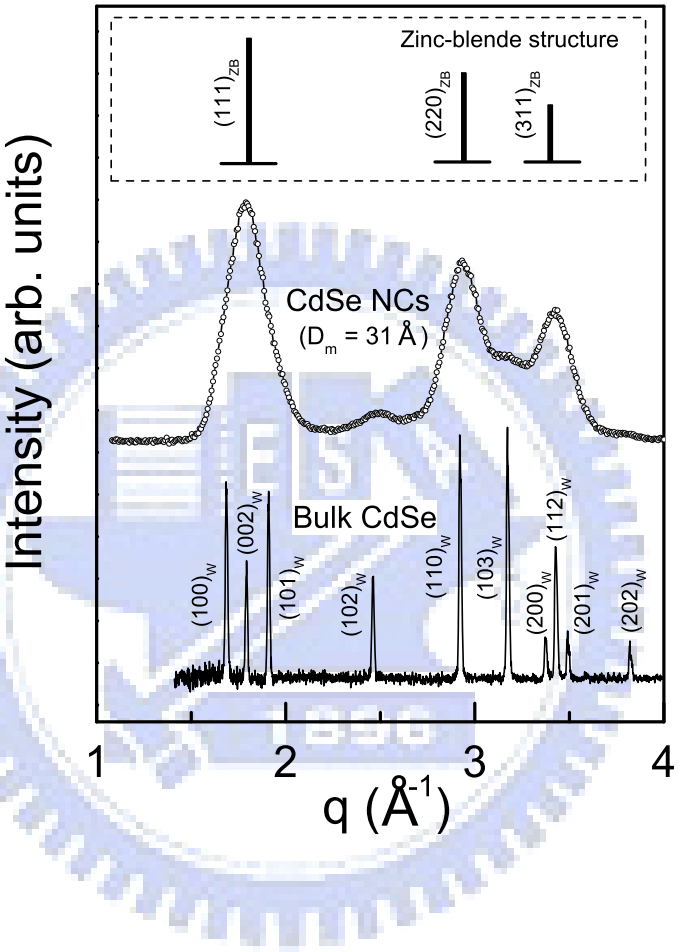

FIG. 3.1: Powder X-ray diffraction spectra of bulk CdSe and CdSe NCs with mean diameter of 31 Å are plotted together with the bulk zinc-blende peak positions for comparision.

Powder XRD patterns of NC samples were simulated with a discrete form of the Debye formula [9]:

$$I(q) = \sum_i \sum_j f_i f_j \frac{\sin(qr_{ij})}{qr_{ij}} \exp\left[-\frac{\sigma^2 q^2}{2}\right], \tag{3.1}$$

in which f_i is the atomic form factor of atom i, r_{ij} is the distance between atoms i

and j, $\exp[-\sigma^2 q^2/2]$ is the Debye-Waller (DW) factor, and σ^2 is the atomic mean-square displacement (MSD). Thermal motion reduces diffraction intensity, and a single average value of the MSD was obtained from a fit of the theoretical patterns to the appropriate data. Thermal damping of EXAFS is associated with the mean-square relative displacement (MSRD) of atom pairs. MSD and MSRD are not identical because in MSRD the vibrations of an absorbing atom and its neighbors are correlated, particularly at low frequencies [12]. Hence, the MSRD is less than a sum of individual atom MSDs [13].

The Debye formula automatically averages over the different cluster orientations in the sample. The major approximation comes from the atomic scattering factors which are calculated using Hartree-Fock wave functions by Cromer and Mann [14]. These scattering factors are used for isolated atoms and thus do not allow for a change of shape of the valence electronic cloud due to chemical bonding. This approximation is acceptable since there are many more core electrons than bonding electrons in Cd and Se. We have also neglected to include the anomalous scattering factors and the incoherent or Compton scattering. The anomalous scattering factors are small corrections which arise due to discontinuities in atomic X-ray absorptions, while Compton scattering results in a diffuse background which is small in the q range studied.

All essential structural features such as size and shape of particle, lattice distortion, disorder and reconstruction/relaxation of surface atoms, and stacking faults/layer-stacking sequences (polytypic structure) [11] were explicitly taken into account since they are intrinsic parameters of the NC model. The position of the atoms in the particle is systematically generated in the WZ and ZB structures, and only those atoms falling inside the outlined ellipsoids are used for the simulation. The dimensions of the ellipsoid were determined by TEM

measurements. Thermal effects are simulated by the introduction of a DW factors. The DW factor does not change peak positions and only affects peak intensities through an exponential damping as q increases.

Both the WZ and ZB structures are based on the stacking of identical two-dimensional planar units translated with respect to each other, in which each atom is tetrahedrally surrounded with four nearest neighbors. The layer stacking is described as ABABAB… along the [001] axis for WZ and as ABCABC… along the [111] axis for ZB. We adopted the polytypic structures composed of WZ and ZB layer stackings to obtain acceptable fits of the experimental data. These sequences represent the presence of several stacking faults in the WZ (or ZB) structure that have been observed also with TEM [10].

Figure 3.2 shows a measurement on CdSe NCs passivated with TOPO/HDA overplotted with the calculated patterns of 31 Å NCs with the WZ and ZB structures as well as bulk lattice parameters. The calculated patterns of defect free WZ and ZB crystallites do not reproduce the overall shape of experimental spectrum, especially for the (102) and (103) peaks. All peaks have a slight shift with respect to the calculation, indicating the presence of a lattice distortion. If a single stacking fault near the particle center is involved in the WZ calculation, it mainly leads to broadening and attenuation in the (102) and (103) peaks and the calculation exhibits a better correspondence to the measured spectrum. The (110) spacing is present in both the WZ and ZB structures and is thus unaffected by the presence of stacking faults along (002) axis. Crude determination of particle size by the Scherrer formula should adopt the width of (110) peak rather than the convolution of the (100), (002), and (101) reflections found in the first diffraction feature.

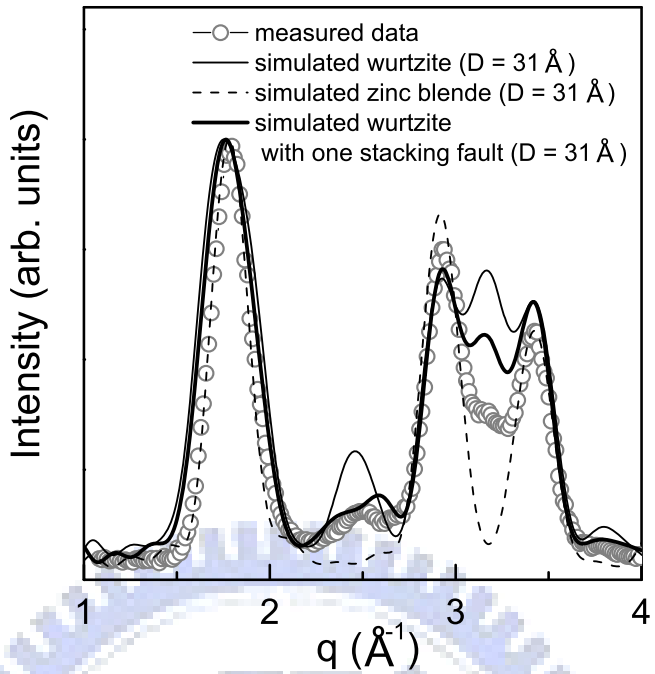

FIG. 3.2: Powder diffraction pattern of TOPO/HDA-passivated CdSe NCs and the calculated patterns for wurtzite and zinc-blende NCs with size of 31 Å.

Figure 3.3 represents experimental diffraction spectra of three CdSe NCs dependent on the particle size as well as the simulated spectra using the Debye formula. We have scaled the simulated spectra to match the experimental intensity of the first peak at $q \approx 1.8$ Å^{-1} and take these spectra as reference points and analyze the effects of thermal motion, stacking faults, and modification separately. Since X-ray scattering is a coherent structural technique, the shape of the simulated spectra is somewhat sensitive to the stacking sequence. We thus tested all possible sequences to achieve the satisfactory fit. For each spectrum the structure shown in Fig. 3.3 is one of the stacking sequences used to have the best fits. We note that the diffraction spectra are dependent on the particle size, which exhibit the increasing density of stacking faults, with the reduction in size, from an observation of the decreasing intensity in the $(102)_{WZ}$ at $q \approx 2.5$ Å^{-1} and

$(103)_{WZ}$ reflections at $q \approx 3.2$ Å^{-1}. The intensities of these two reflections are sensitive to the number of stacking faults since they do not exist in the ZB structure.

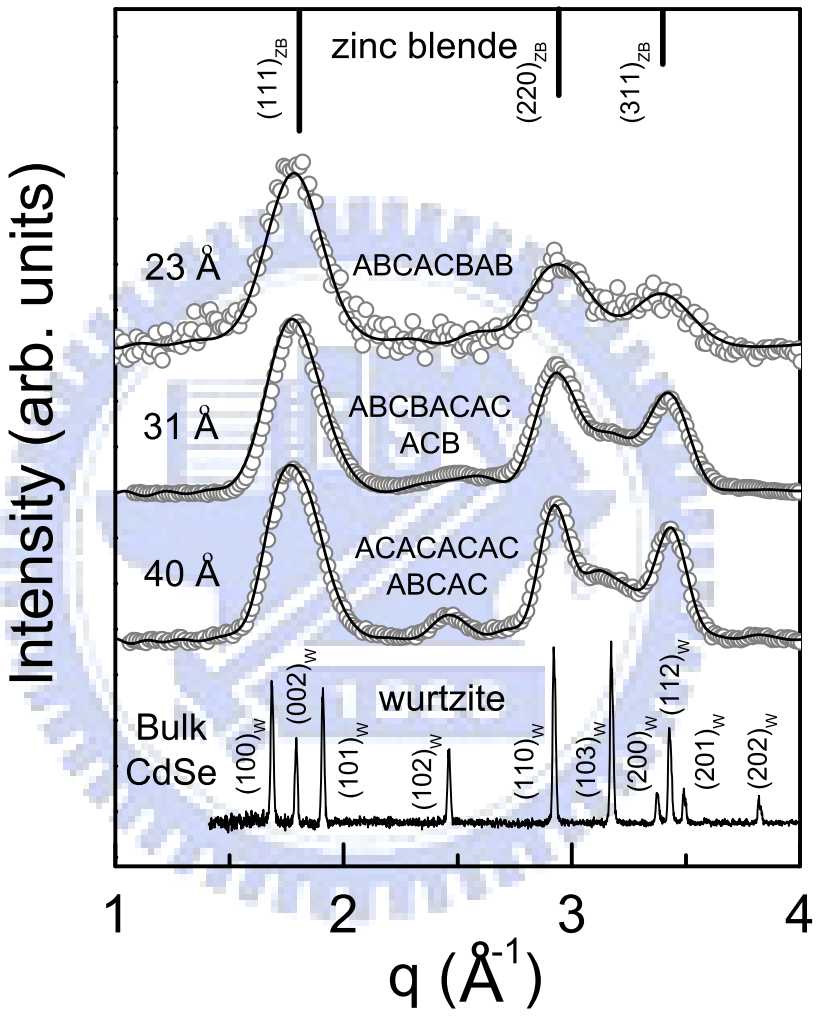

FIG. 3.3: Experimental diffraction spectra of bulk CdSe and three CdSe NCs as well as the corresponding simulations by Debye formula.

Figure 3.4 shows the fraction of WZ stacking in NCs as a function of their size and the picture for estimation of stacking fraction. The fraction of WZ

stacking is estimated by the ratio of WZ to (WZ+ZB) stacking. In the case shown in the inset of Fig. 3.4, for example, the WZ stacking fraction is 0.56 for a cylindrical shape and is 0.61 for an ellipsoid shape. The result reveals that WZ layer stacking increases with size, which is accompanied with some enhanced features that appear only for the WZ structure [see, for example, the $(102)_{WZ}$ and $(103)_{WZ}$ reflections in Fig.3.3]. The stacking sequences indicated in Fig.3.3 are not unique: similarly satisfactory fits of the experimental data can be achieved for other stacking sequences, which, nevertheless, yield similar values of WZ stacking fractions in NCs.

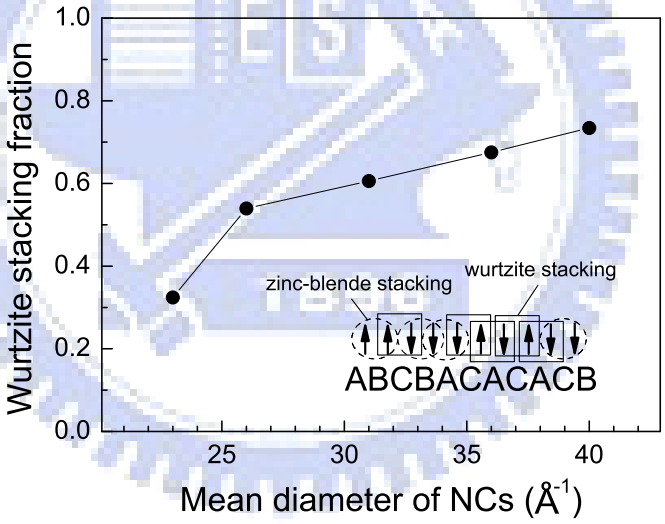

FIG. 3.4: The wurtzite stacking fraction as a function of the NC mean diameter as well as the picture for estimation of stacking fraction.

3.3 Diffraction patterns fitted with a simple model

In order to obtain the quantitative structural parameters by strict fit, we proposed a simple model based on several conditions and approximations listed

in the following:

1. The particle shape is an ellipsoid.
2. Each NC has a defect-free structure.
3. The diffraction feature is a linear combination of the reflections for x WZ and $(1-x)$ ZB NCs.
4. A tetrahedron of WZ structure has the same distortion as that of ZB structure; the change in peak position due to this structural distortion should thus be considered.
5. All peak positions follow

$$q_{hkl}^{W} = 4\pi\sqrt{\frac{h^2+hk+k^2}{3a_W^2}+\frac{l^2}{4c_W^2}}\text{, for WZ structure;} \tag{3.2}$$

$$q_{hkl}^{ZB} = 4\pi\sqrt{\frac{h^2+k^2+l^2}{3a_{ZB}^2}}\text{, for ZB structure.} \tag{3.3}$$

For simplicity, we consider that each NC has an ellipsoid shape and possesses WZ or ZB structure without stacking fault. Because stacking fault can lead to WZ (ZB) transforming into ZB (WZ) structure near the fault plane, the ratio of WZ to ZB reflection intensities would exhibit the density of stacking faults.

For an ellipsoid shape of particle, three axes are of lengths L_a, L_b, and L_c, respectively, in which $L_a = L_b$. For diffraction from such particle of finite size, we can derive that for any (hkl) reflection the peak width in q space (Appendix A) is

$$W_{hkl} = 2\pi\sqrt{\frac{\frac{h^2+hk+k^2}{3a^2}+\frac{l^2}{4c^2}}{\frac{h^2+hk+k^2}{3a^2}L_a^2+\frac{l^2}{4c^2}L_c^2}}, \tag{3.4}$$

in which a and c are the WZ lattice parameters. Since the (111), (220), and (311) reflections in ZB structure correspond to the (002), (110), and (112) in WZ

structure, respectively, these ZB peaks have the same width as the corresponding WZ peaks. The intensity of each reflection was determined by the atomic form factor and the peak profile was characterized by a Gaussian function. Therefore, the total intensity is a combination of the contributions from WZ and ZB NCs, which can be expressed as

$$I_{tot}(q)=\frac{1}{q^2}\left\{I_W\sum_{hkl}N_{hkl}\left|F_{hkl}^{W}\right|^2\exp\left[-\frac{1}{2}\left(\frac{q-q_{hkl}^{W}}{W_{hkl}}\right)\right]+I_{ZB}\sum_{hkl}N_{hkl}\left|F_{hkl}^{ZB}\right|^2\exp\left[-\frac{1}{2}\left(\frac{q-q_{hkl}^{ZB}}{W_{hkl}}\right)\right]\right\}$$

$$\exp\left(\frac{-\sigma^2q^2}{2}\right)+BG \qquad (3.5)$$

in which N_{hkl} is the multiplicity, F_{hkl} is the atomic form factor, $\exp[-\sigma^2q^2/2]$ is the DW factor, σ^2 is the atomic MSD, and BG is the background. To check whether the lattice parameters from fits are reliable, we have tried to fit the simulated powder XRD patterns, using the Debye formula, of nanocrystals with distorted unit cell. The fitting results show a small deviation of ±0.002−0.006 Å from the parameters used in simulation for different particle sizes.

The measured diffraction patterns of TOPO/HDA-passsivated CdSe NCs are shown in Fig. 3.5, along with the corresponding fits. We can see that the fit results reveal an increasing intensity in $(102)_{WZ}$ reflection with increasing particle size, reflecting an increasing WZ stacking. The fit intensities of reflections in some ranges do not reproduce the experimental data very well, this may be due to the effect of surface modification which is not included in our fit. In the fitting model, we considered the DW factor, which describes the thermal effect, to have a satisfactory fit in the range of higher q. We found that the DW factors obtained by fits are consistent with those used in simulations by the Debye formula.

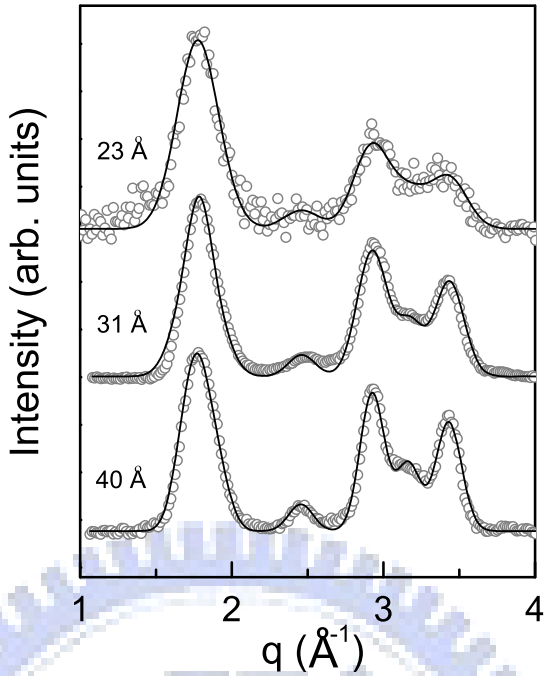

FIG. 3.5: Powder X-ray diffraction patterns of CdSe NCs and the corresponding fits.

The lattice parameters c_{NC} and a_{NC}, presented in Fig. 3.6, are obtained from fits of the diffraction patterns of CdSe NCs. It should be noted that we here consider ZB structure along the (111) direction has the corresponding lattice parameters *c* and *a* of WZ structure along the (002) direction. For bulk CdSe, the lattice parameters we measured are c_b = 7.01 Å and a_b = 4.299 Å and are consistent with the values in data base [15] and other report [16]. Our results show that a decreasing particle size is correlated with an expansion in c_{NC} and a contraction in a_{NC} relative to bulk values, indicating a nonuniform distortion of the unit cell, as also found for CdS particles [17]. The structural distortion and, in particular, the decreased volume of the unit cell of NCs (see the inset of Fig. 3.6) are attributed to an increased ratio of surface to volume with decreasing NC size.

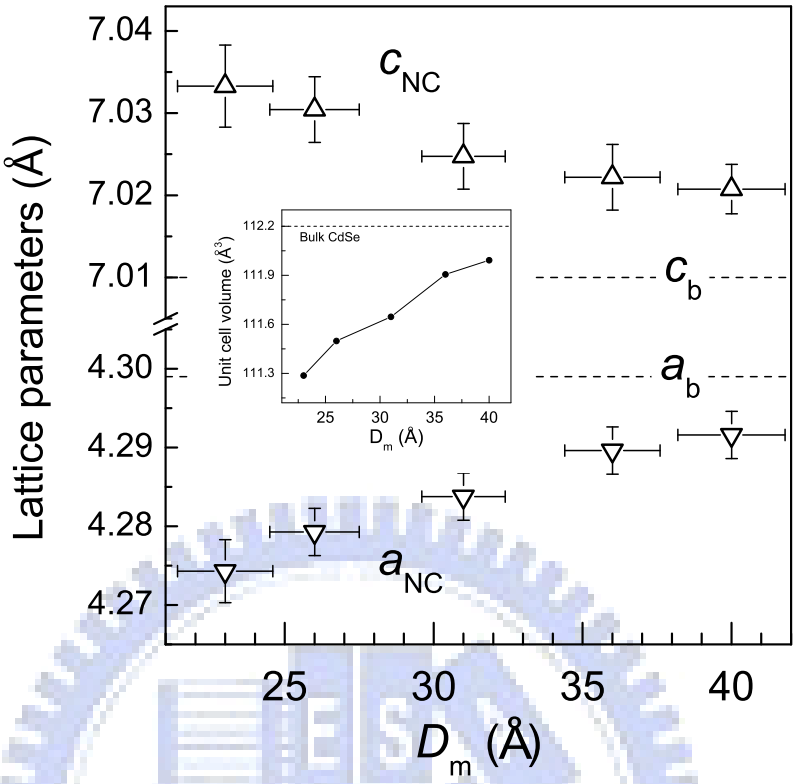

FIG. 3.6: Size-dependent lattice parameters of CdSe NCs determined by fit of powder XRD data. The lattice parameters of bulk CdSe, c_b and a_b, are indicated. Inset: the unit cell volume as a function of particle size.

3.4 EXAFS studies on bond lengths

3.4.1. Structural properties of CdSe nanocrystals observed by EXAFS

The k^3-weighted Cd and Se *K*-edge EXAFS spectra for bulk CdSe and three NCs, measured at room temperature, are shown in Fig. 3.7. A couple of qualitative trends can be observed without any detailed data analysis. Firstly, the progressive increase of the oscillation period indicates the mean Cd−Se bond length contracts with decreasing particle size, which is accompanied by a

reduction in coordination number and larger structural disorder (reflected by smaller amplitude and broader oscillations). Secondly, the variation of Se *K*-edge spectra among different samples is less noticeable with respect to that of Cd *K*-edge spectra. It implies that most Se atoms are located in the interior of nanocrystals and the CdSe core is predominantly stabilized by Cd−surfactant submonolayer. Thirdly, all spectra seem to be composed of oscillations with single frequency, implying that EXAFS is dominated by the contribution from the first coordination shell. The absence of second- and higher-shell contributions in EXAFS spectra will be discussed in the following paragraphs.

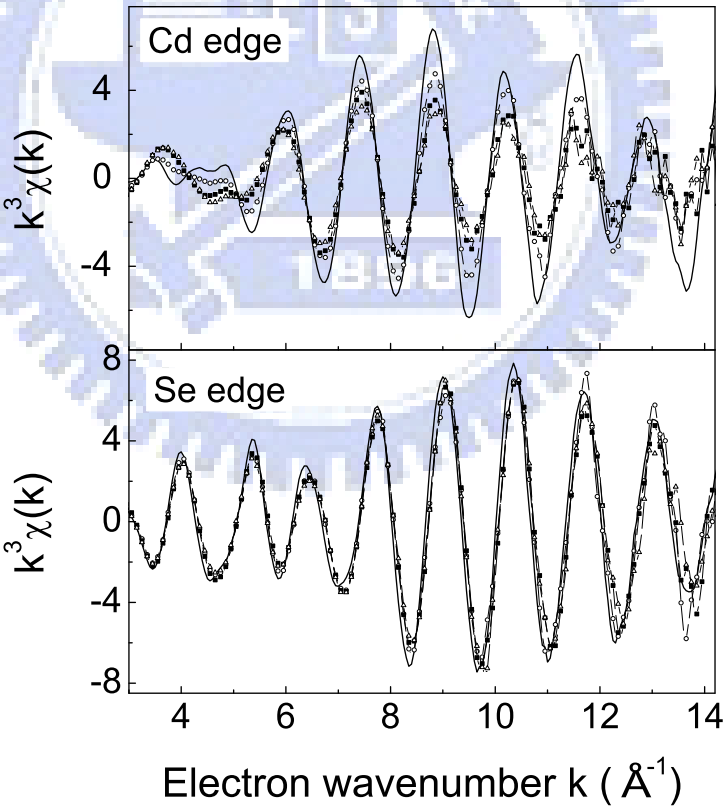

FIG. 3.7: k^3-weighted (a) Cd and (b) Se *K*-edge EXAFS spectra of bulk CdSe (solid line) and NCs with mean diameters of 40 (–○–), 32 (–■–), and 23 Å (–△–).

Figure 3.8 represents the Fourier transformed EXAFS spectra for bulk CdSe and three nanocrystals. We find that the second shells of the bulk CdSe as well as the NC samples are completely absent. As have been observed by A. C. Carter *et al*. [18], however, the second shell of the bulk CdSe was clearly visible at 80 K. Therefore, the absence of an observation in higher-shell contributions, even for bulk sample, indicates a rather large thermal component in the bulk second-shell Debye-Waller factor.

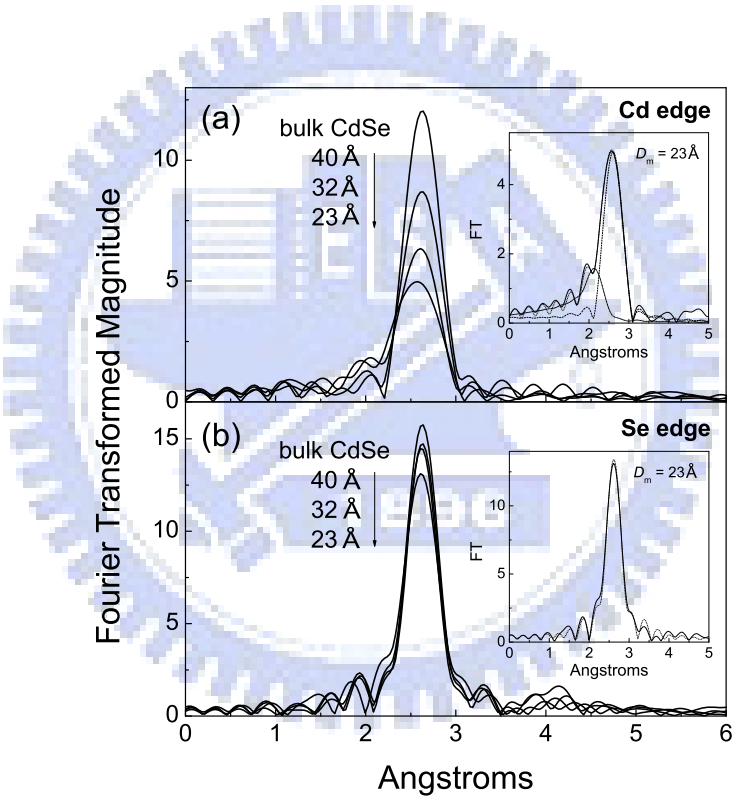

FIG. 3.8: Fourier tranforms of (a) Cd and (b) Se *K*-edge EXAFS spectra for bulk CdSe and three-sized nanocrystals. The insets show the fits of the respective FTs spectra of the smallest nanocrystals with 23 Å size, where solid lines are the experimental data and dot lines the fitting results.

The reduced peak height in Fourier transforms (FTs) for nanocrystals relative to the bulk sample indicates a drop in coordination number, which results from

surface truncation. A comparison between Figs. 3.8(a) and 3.8(b) reveals that the peak height of Cd *K*-edge data reduces more dramatically than that of Se *K*-edge data as the particle size decreases, as we observed in Fig. 3.7. This observation implies that the Cd atoms are slightly rich at the NC surface, especially for the smaller particles.

In spite of a large influence by thermal effect, we observed a slight broadening in peak width of the first shell for the NC samples, indicating only a small disorder in bond length. Moreover, a relatively low energy is required to induce bond bending comparable to the variation in bond length. Hence, it is deemed that the bond angle disorder is the dominant contribution for the complete absence of high-shell peaks.

The inset of Fig. 3.8(a) illustrates the fit to Fourier transformed EXAFS spectrum at Cd *K*-edge of the 23 Å nanocrystal in the range from 1.5 to 3.3 Å. The side lobe at lower k has an asymmetric profile with respect to the main contribution of Cd−Se. It is ascribed to the Cd−surfactant bonds at the nanocrystal surface. This argument verifies that the Cd−O/N layer appears on the nanocrystal surface and the Cd−Se bonds show mainly the interior properties. The inset of Fig. 3.8(b) shows the fit to the Se *K*-edge EXAFS spectrum for the 23 Å nanocrystals. A good fit can be obtained, though only Cd atoms were considered as the nearest neighbors around Se atom. This also indicates that no impurities or not-reacted precursors such like free TOPSe are left in the samples.

Fig. 3.9 shows fits to the single-shell filtered data of $\chi(k)*k$ of 23 Å nanocrystals. For Cd edge solid line represents the fitting result with both the nearest Se atoms and terminated atoms of capping molecules around Cd atom taken into account. For Se edge, in contrast, only the nearest Cd atoms around Se atom were necessary to achieve a satisfactory fit. We had tried to fit Cd

K-edge data without considering the contributions from low Z atoms, but a poor result was obtained in low *k* region. This implies that Cd atoms should have the neighboring atoms with low atomic number, such as O or N atoms under the

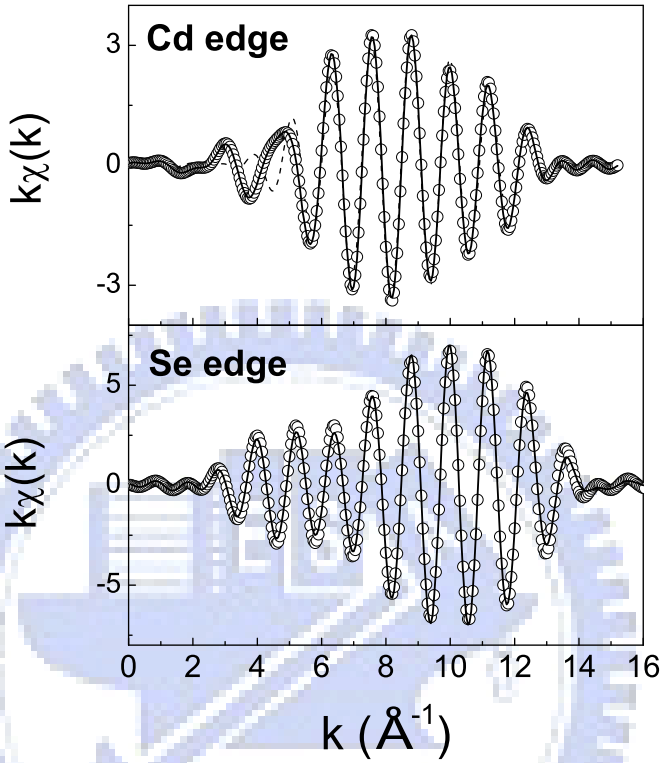

FIG. 3.9: Fourier filtered EXAFS spectra (open circles) and the best fits (solid lines) of CdSe NCs with the size of 23 Å at Cd and Se *K*-edge over the range 1.5−3.3 Å in *r* space. A poor fit (dashed line) obtained by considering merely the Se atoms as the nearest neighbors of the Cd atom is also plotted.

consideration of our synthesis condition. However, equally good fits are achieved by individually considering O and N coordination so that we cannot determine if the surface Cd atoms bonded to TOPO or HDA, or both. In addition, attempts to fit this spectrum with the replacement of O/N by P (the terminal atom of TOP) result in poor fits with unreliable structural parameters, verifying that Cd atoms have Se and O/N as the nearest neighbors. For Se *K*-edge data of

nanocrystals, a good fit with only Cd backscatters can be obtained, indicating the absence of bonding between the surface Se atoms and the surfactants.

In addition to the data of bulk CdSe and NCs taken at room temperature, the Se *K*-edge EXAFS of NCs were also measured at the temperature of ~10 K as shown in Fig. 3.10. The spectrum also reveal the lack of contributions from higher shells, as observed in Fig. 3.8, reflecting that there is a significant static disorder in the tetrahedral bond angle in the interior of the NCs as well as at the surface.

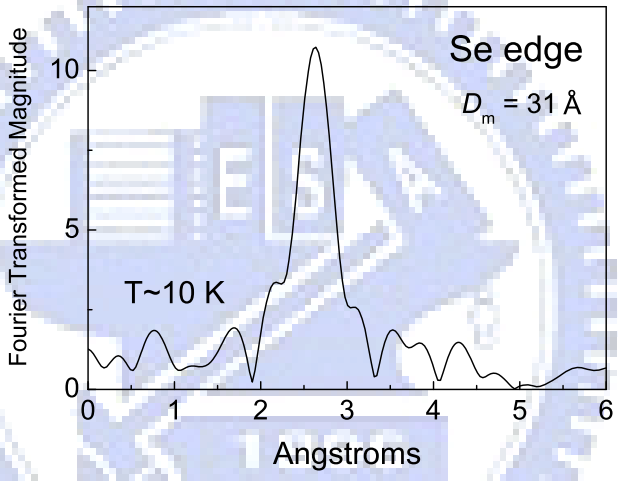

FIG. 3.10: Fourier tranforms of Se *K*-edge EXAFS spectra, measured at ~10 K, for CdSe NCs with mean diameter 31 Å.

Figure 3.11 displays a comparison between the measured coordination number of five NCs with the uncertainty and the results calculated by the ball-and-stick model. The Cd coordination number around Se atoms is in good agreement with the calculation and is always larger than the Se coordination number around Cd atoms, suggesting that the surface of nanocrystals are mostly occupied by Cd atoms as mentioned above. The sum of the coordination numbers of the Se and O/N around the Cd atoms is approximately 5.0 (see Table

I), denoting more than one O or N atom bonded to each surface Cd atom. This is probably due to the surface disorder, which can create more unoccupied orbitals for the surface atoms to form bonding with organic ligands. It is worth to note that the total coordination of Se and water group around Cd is larger than that of 3.9 reported in the literature [18]. We assume that is because the NCs are synthesis dependent, and the chemical structures of the surfactants used in our work are quite different. In comparison, the coordination numbers of Se *K*-edge data are varying in the range of 3.3−3.5. This indicates that some Se atoms located at the NC surface are not bonding to the organic ligands.

TABLE 3.1: Structural parameters derived from EXAFS spectra of CdSe nanocrystals

Cd *K*-edge results

NC size	N_{Cd-Se}	R_{Cd-Se}	$\Delta\sigma^2$	$N_{Cd-O/N}$	$R_{Cd-O/N}$	$\Delta\sigma^2$
23	2.53	2.607	0.00724	2.63	2.245	0.01397
30	2.71	2.609	0.00692	2.38	2.235	0.01361
32	2.77	2.611	0.00687	2.25	2.219	0.01311
36	2.98	2.612	0.00667	1.81	2.210	0.01487
40	3.51	2.618	0.00636	1.34	2.205	0.01743

Se *K*-edge results

NC size	N_{Se-Cd}	R_{Se-Cd}	$\Delta\sigma^2$
23	3.49	2.609	0.00552
30	3.37	2.611	0.00526
32	3.54	2.612	0.00557
36	3.41	2.614	0.00532
40	3.47	2.618	0.00535

The nanocrystal size and mean interatomic distance R are expressed in units of angstrom (Å).

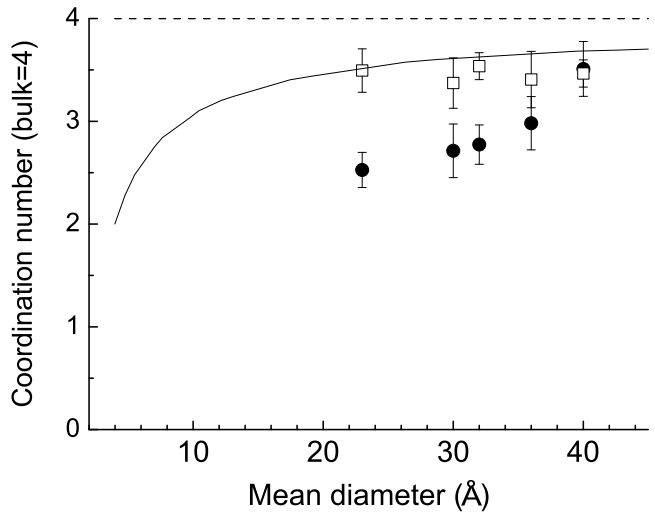

FIG. 3.11: The measured first-shell coordination numbers of five NCs are plotted with the calculated values by the ball-and-stick model (solid curve). Solid circles indicate the Se coordination numbers around Cd atoms and open squares Cd coordination numbers around Se atoms.

The Cd−Se and Cd−O/N bond lengths as a function of particle size determined by Cd *K*-edge EXAFS data of NCs, wurzite bulk CdSe as well as Cd−OA/TOPO/HDA are compared in Fig. 3.12. It is obvious that the interior Cd−Se and the surface Cd−O/N exhibit an opposite size-dependent behavior of their bond lengths. With the reduction of particle size, mean Cd−Se bond length has a contracted tendency with respect to bulk CdSe, corresponding to the slight shift of diffraction peak toward higher angle. This bond length contraction has also been reported previously in an EXAFS study [18]. In contrast, the surface Cd−O/N bonds show a slight size-dependent expansion and gradually approach to the bond length of Cd−OA/TOPO/HDA. In conjunction with the mechanism of the heteroepitaxial like growth [19], CdSe NC passivated with TOPO/HDA resembles the CdSe core partially surrounded by the Cd−TOPO/HDA monolayer to form a core-shell system. The lattice mismatch between the

interior CdSe and the surface Cd−O/N layer leads to the contraction and expansion in the interatomic distance of the Cd−Se and Cd−O/N bonds, respectively, for minimizing the strain energy at the surface. This expansionary behavior implies that the structure of the surface Cd−O/N layer for smaller particles is much similar to that of Cd−OA/TOPO/HDA with respect to larger ones due to the surface roughness and disorder. However, the size-dependent contraction in the bond length of Cd−O/N we observed is opposite to the similar systems reported elsewhere [18]. A possible reason is that no hindering is given to prevent the NC surface layer to minimize its free energy due to the weaker steric interactions between TOPO/HDA ligands.

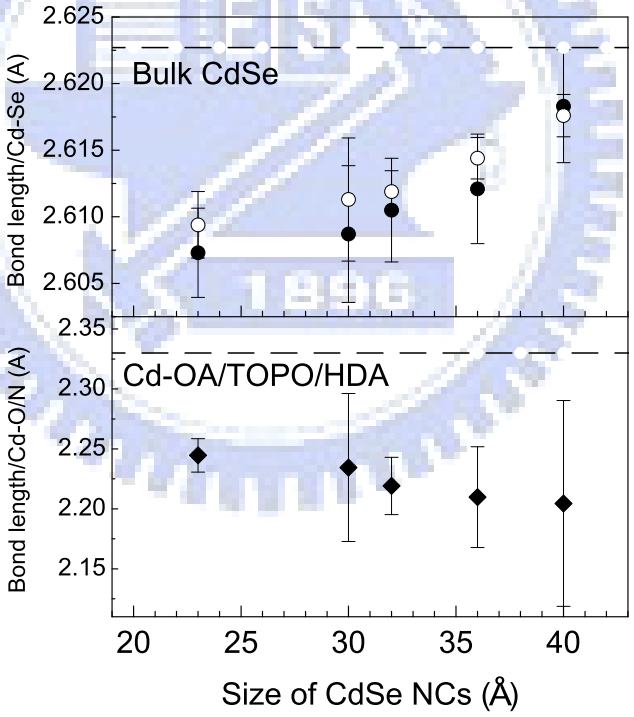

FIG. 3.12: Mean length of the Cd−Se and Cd−O/N bonds for CdSe nanocrystals with various particle sizes. Solid circles represent the mean Cd−Se bond length obtained from Cd *K*-edge EXAFS and open circles from Se *K*-edge EXAFS. Solid diamonds show the mean Cd−O bond length obtained from Cd *K*-edge EXAFS. Dash lines plotted in upper and lower figures are the bond lengths of Cd−Se and Cd−O/N measured from bulk CdSe and Cd precursor (Cd−OA/TOPO/HDA) for references, respectively.

3.4.2. Distinct bond lengths $R^{(1)}$ and $R^{(2)}$

For a WZ structure, bonds between nearest-neighbor anion and cation for a tetrahedral structure have two distinct lengths (see Fig. 3.13). The length of the axial bond, along the *c* axis, is defined as $R^{(1)} = uc$; three other bonds have equal length $R^{(2)} = a\sqrt{1/3 + (1/2 - u)^2 (c/a)^2}$, in which u denotes the dimensionless internal-cell structural parameter [20]. In an ideal WZ structure for which $c/a = \sqrt{8/3}$ and $u = 3/8$, the bond lengths are equal [$R^{(1)} = R^{(2)}$]. We used the above expressions with lattice parameters obtained from the fit of XRD data and applied a restriction on the coordination number $3N_{R^{(1)}} = N_{R^{(2)}}$ to fit all Se *K*-edge EXAFS spectra; in addition, the DW factors of these two bond lengths were constrained to be the same.

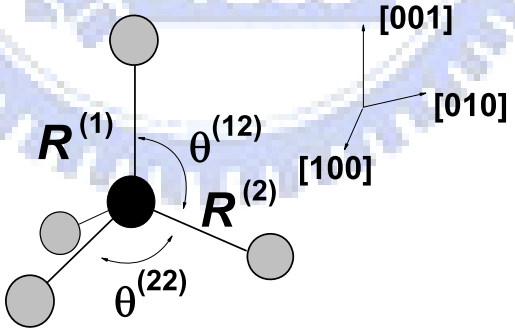

FIG. 3.13: The scheme of a tetrahedral structure indicates the axial bond length $R^{(1)}$, the equatorial bond length $R^{(2)}$, and the bond angles $\theta^{(12)}$ and $\theta^{(22)}$.

Figure 3.14 shows the first-shell filtered data, measured at a temperature of ~10 K, of $\chi(k)*k$ of three NCs and a bulk CdSe sample together with the corresponding fits in all three NCs. Satisfactory fits with only Cd backscatter

were achieved, indicating that Se has only Cd as its nearest-neighboring atoms. Of three qualitative trends that we observed, the progressive increase of the oscillation period indicates that the mean Cd−Se bond length contracts with decreasing particle size, which is accompanied by a broadening due to larger structural disorder; the variation of Se *K*-edge spectral amplitude among samples is less noticeable (Fig. 3.7), reflecting that most Se atoms are located in the interior of NC, and all spectra seem to be composed of oscillations with a single frequency, indicating that EXAFS is dominated by the contribution from the first coordination shell the same conclusion as our RT data discussed previously.. Since the surface Cd atom has not only Se but O and/or N as its nearest neighbors, we focus on Se *K*-edge EXAFS from Cd−Se pairs to prevent the unnecessary fitting deviation.

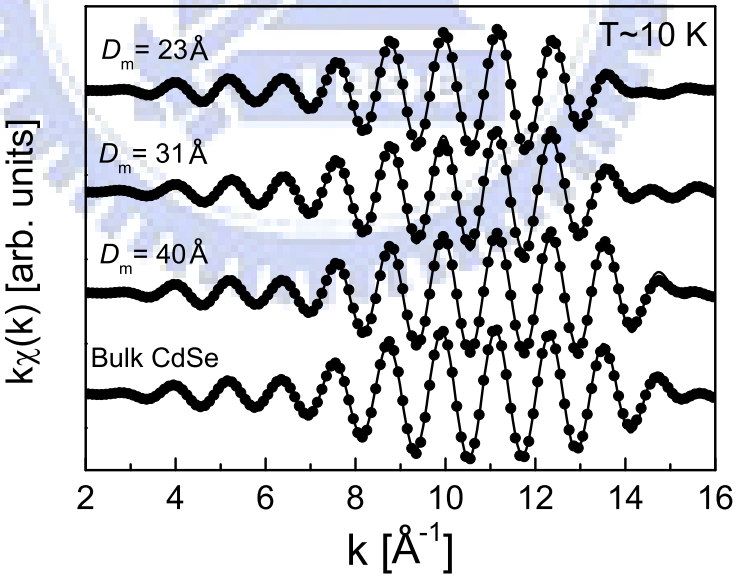

FIG. 3.14: Single-shell filtered Se *K*-edge data (symbols) measured at the temperature of ~10 K and the corresponding fits (lines) by considering the contributions of $R^{(1)}$ and $R^{(2)}$. The NC and bulk CdSe data were filtered over an identical range 1.5–3.3 Å in *r* space.

The distinct bond lengths $R_{NC}^{(1)}$ and $R_{NC}^{(2)}$ normalized to those of bulk CdSe obtained from the fit of the Se *K*-edge EXAFS data are plotted in Fig. 3.15,

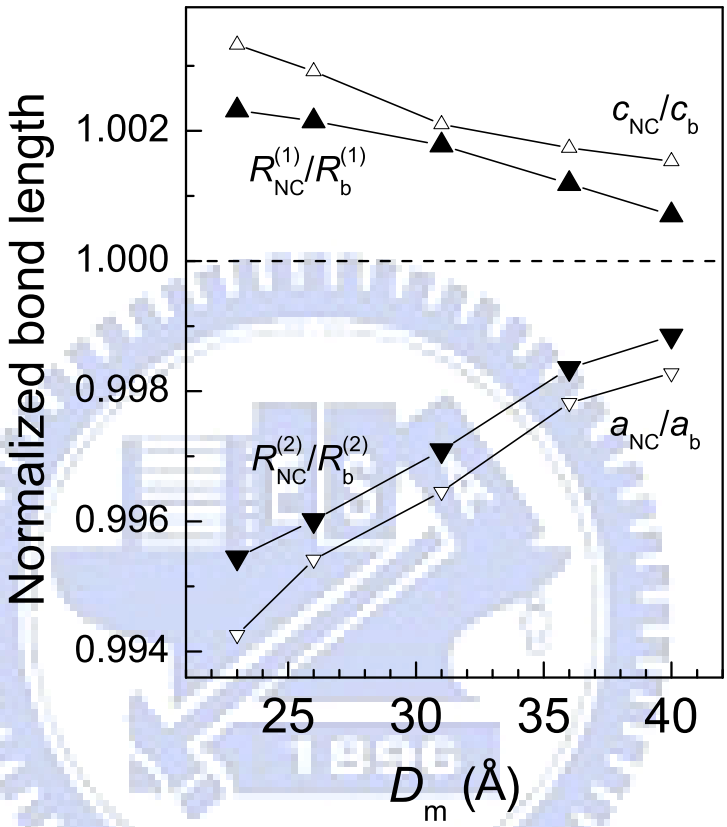

FIG. 3.15: Size dependence of normalized bond lengths, $R^{(1)}$ and $R^{(2)}$, for CdSe NCs passivated with TOPO/HDA is plotted together with the normalized lattice parameters, *c* and *a*.

along with lattice parameters for comparison. A schematic diagram of an atomic tetrahedron is shown in the inset. $R^{(1)}$ has a tendency to expand whereas $R^{(2)}$ exhibits a contraction as NCs become smaller. $R_{NC}^{(1)}/R_b^{(1)}$ and $R_{NC}^{(2)}/R_b^{(2)}$ show a size dependence similar to c_{NC}/c_b and a_{NC}/a_b, respectively. This observation implies that the structural parameter *u* remains almost constant (~0.384) even for

small NCs. According to the variations of $R^{(1)}$ and $R^{(2)}$, the axial bond angle $\theta^{(12)}$ of a tetrahedral structure (see Fig. 3.13) becomes larger with decreasing size, whereas the equatorial bond angle $\theta^{(22)}$ reveals an opposite behavior.

Figure 3.16 shows the measured *u* in this study and the theoretical calculation [8] and ideal value are also plotted for comparison. We find that the measured parameters *u*, even for bulk CdSe, are larger than the theoretical and ideal values, though the lattice parameters *a* and *c* are quite similar to the calculated results. The larger u is related to that the axial bond length $R^{(1)}$ we measured is observably larger compared to the predicted value for CdSe [8]. In addition, the parameter *u* is independent of particle size, as we mentioned above.

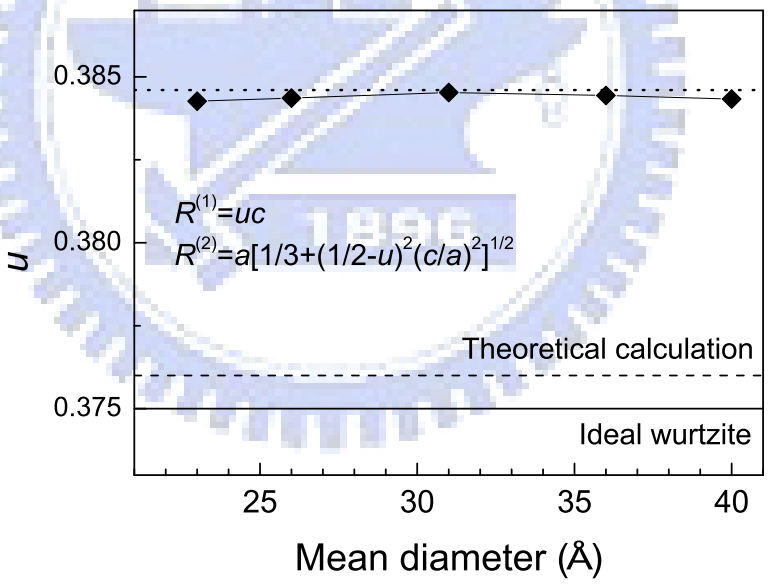

FIG. 3.16: The structural parameters *u* as a function of mean diameter for CdSe nanocrystals. The calculated and ideal wurtzite values are indicated.

3.5 Discussion

3.5.1. *Variation in bond lengths $R^{(1)}$ and $R^{(2)}$*

The change in lattice parameter of a spherical cluster compared to that of the bulk can be related to the surface stress through the concept of the surface pressure, following the modified Laplace law for solids [5,21]:

$$P = \frac{4\Gamma_s}{D}, \tag{3.7}$$

in which P is the pressure, D is the particle size, and Γ_s is the surface stress. In the elastic strain domain, the isostatic volume stress P, is related to the relative parameter difference, following:

$$P = \frac{E}{1-2\nu}\left(\frac{a_{NC}-a_b}{a_{NC}}\right), \tag{3.8}$$

in which E is the Young modulus [41.5 GPa for CdSe (Ref. 22)] and ν is the Poisson coefficient [0.37 for CdSe (Ref. 22)]. Meulenberg *et al*. [7] reported that the measured stress of CdSe NCs, using resonance Raman spectroscopy, is related to surface passivation: CdSe NCs passivated with HDA exhibit the size-dependent compressive stress, which can lead to a contraction of lattice; this is because the HDA-capped NCs behave similarly to perfect spheres with very little influence from the HDA surfactant layer. For CdSe NCs passivated with TOPO, on the other hand, the results show tensile stress giving rise to lattice expansion and do not follow a smooth functional relationship ($P \approx -0.53$ GPa in average); they proposed that the TOPO-capped NCs have a strong interaction between the surface Cd atoms and TOPO ligands, leading to an outward surface modification.

The variations of the lattice with size for CdSe NCs passivated with HDA and TOPO, deduced from Ref. 7, are plotted in Fig. 3.17 to compare with our results.

The size-dependent $R_{NC}^{(2)}/R_b^{(2)}$ and a_{NC}/a_b apparently reveal some combined effects of stress from TOPO and HDA surfactants, with a net decrease. This result suggests that the surface atoms of as-prepared CdSe NCs are attached to both TOPO and HDA molecules, supporting our EXAFS studies. According to the modified Laplace law, the continuous decrease in a_{NC} with decreasing NC size reflects the increasing surface pressure and surface stress.

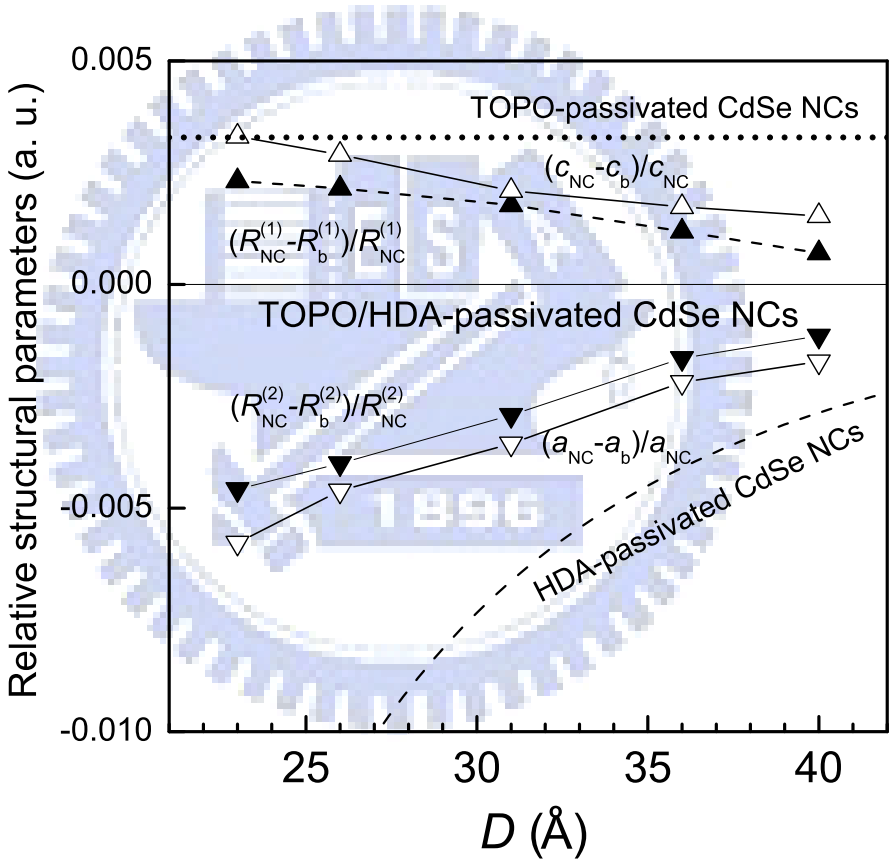

FIG. 3.17: Relative structure parameters of CdSe NCs dependent on particle size. The dotted and dashed lines represent the relative structural parameters as a function of particle size for CdSe NCs passivated with TOPO and HDA (deduced from Ref. 7), respectively.

Different from $R_{NC}^{(2)}$ and a_{NC}, however, $R_{NC}^{(1)}$ and c_{NC} becomes expanded

compared to bulk CdSe (R_b). The relaxation of the atomic positions at a stacking fault interface can result in an increase of the bond length normal to the fault plane, which was reported for bulk AlN and GaN using *ab-initio* calculations [23]. As shown in Fig. 3.4, moreover, the small NCs possess the higher density of stacking fault. The observed expansion in $R_{NC}^{(1)}$ and c_{NC} of CdSe NCs may be induced by two competing effects of surface modification driven by surface stress and atomic relaxation due to stacking faults. We note that, nevertheless, the overall effect of the surface pressure or stress is still compressive, leading to a volume decrease of the unit cell with decreasing size.

3.5.2. *Surface energy of TOPO/HDA-passivated CdSe nanocrystals*

According to Ref. 5 the surface stress Γ_s is related to the surface tension γ and the surface strain ε_s following, $\gamma = \Gamma_s \varepsilon_s / 2$, where the surface strain ε_s is given by $\Gamma_s = E_s \varepsilon_s / d_a$. E_s is the surface elastic modulus approximated by $E_s = (2/3)E$ and d_a is the atomic density perpendicular to the surface that is, $1/d_a = 2r_a$ the atomic diameter. The surface tension, by combining Eq. (3.7) with Eq. (3.8), can be expressed as

$$\gamma = 0.1875 \frac{E}{R_{ave}} \left[\frac{D}{2(1-2\nu)} \right]^2 \left(\frac{a_{NC} - a_b}{a_{NC}} \right)^2, \qquad (3.9)$$

in which γ is equal to the surface energy f [21]and R_{ave} is the average value of Cd−Se bond length.

The variation of the surface energy estimated from Eq. (3.9) is plotted in Fig.

3.18. We find that the surface energies, calculated by whatever lattice parameter *a* or *c*, are rather small and approach zero with respect to HDA-passivated CdSe NCs [7], because of the small variation in the relative lattice parameters with particle size (shown in Fig. 3.17). The effect of the surface passivation or molecular adsorption on the thermodynamic behavior of small clusters is known

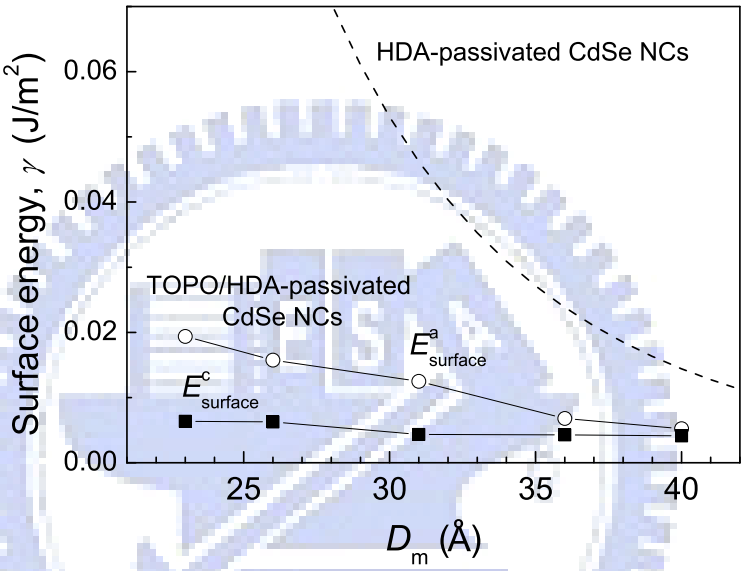

FIG. 3.18: Surface energy of TOPO/HDA-passivated CdSe NCs as a function of size, compared to HDA-passivated CdSe NCs (deduced from Ref. 7). The open dots represent the surface energy $E^a_{surface}$ calculation by lattice parameter *a*, and the solid squares are the surface energy $E^c_{surface}$ calculation by lattice parameter *c*.

to reduce the surface energy [5], hence the obtained surface energy with small value can be attributed to the organic ligands, TOPO and HDA. In addition, the surface energy $E^a_{surface}$, calculated by lattice parameter *a*, has the increasing tendency with decreasing size and is slightly larger than $E^c_{surface}$, calculated by

lattice parameter *c*. This size dependence indicates the slightly increasing $E^{a}_{surface}$. The surface energy $E^{c}_{surface}$, however, has a smaller value compared to $E^{a}_{surface}$ and a rather weak dependence on particle size, owing to the atomic relaxation contributed from stacking faults. Since $f_{ZB} < f_{W}$ for CdSe as discussed above, moreover, an increasing fraction of ZB stacking via stacking faults, with decreasing particle size, can also lower the surface energy.

3.5.3. *Phase transformation of CdSe nanocrystals*

The gradual change in the structural fraction of CdSe NCs, shown in Fig. 3.4, can be related to a continuous phase transformation. P. Perriat *et al*. used a thermodynamic model to describe the phase transition depending on the cluster size [21,24]. Referring to their notions, the chemical/mechanical potential per mole, g^{*}, is defined as $\mu^{0} + 6\gamma\overline{V}/D$, in which μ^{0} is the chemical potential, γ is the surface tension which is turned out to be equal to the surface energy *f* [21], and $\overline{V}$ is the partial molar volume of the constituent of the grain. For bulk CdSe ($D\rightarrow\infty$), The critical temperature T_c of the ZB-to-WZ structural phase transition is about 95 ˚C [25], so that $\mu^{0}_{ZB} < \mu^{0}_{W}$ below T_c and $\mu^{0}_{ZB} > \mu^{0}_{W}$ above T_c. Since the growth temperature of the CdSe NCs was about 270 ˚C larger than bulk T_c, the relation between chemical potentials is $\mu^{0}_{ZB} > \mu^{0}_{W}$. Moreover, CdSe NCs with very small size predominantly possess a ZB structure at any temperature of preparation [10,26], we should assume $\gamma_{ZB} < \gamma_{W}$ (or $f_{ZB} < f_{W}$) to satisfy the experimental results because $g^{*}_{ZB} < g^{*}_{W}$ for small clusters. With the

particle size increasing, g^* is gradually dominated by the chemical potential μ^0; therefore, there would be a possibility of the phase transition from a ZB to a WZ structure, consistent with our observation in Fig. 3.4.

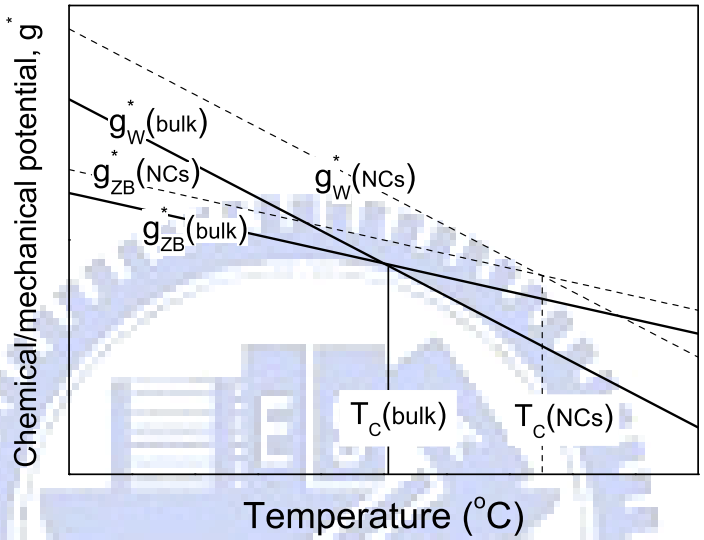

FIG. 3.19: Schematic diagram of the size-dependent phase transition of CdSe.

Figure 3.19 clearly shows a phase transition temperature increasing as decreasing particle size. This result is in correspondence with the direct calculation of the variation of the critical size D_c with temperature [24]:

$$\frac{d}{dT_c}\left(\frac{1}{D_c}\right)=\frac{1}{6\overline{V}^0}\frac{S^0_{ZB}-S^0_W}{\gamma_{ZB}-\gamma_W}, \tag{3.6}$$

in which S^0_{ZB} and S^0_W are the molar entropies of ZB and WZ phases, respectively. The WZ structure is stable at high temperature for CdSe [25], thus it possesses a larger entropy than ZB structure ($S^0_{ZB}<S^0_W$). We can obtain $d(1/D_c)/dT_c \geq 0$, so that T_c increases as D_c decreases.

3.6 Summary

We characterized the structural parameters of TOPO/HDA-passivated CdSe nanocrystals by analyzing powder X-ray diffraction and extended X-ray absorption fine structure spectra. For X-ray diffraction studies, the resulting lattice parameters from fits exhibit an expansion in *c* and a contraction in *a* with reduction in particle size. For extended X-ray absorption fine structure studies, we turned out that Cd atoms are slightly rich at the nanocrystal surface and attached to the organic ligands TOPO and HDA, while the surface Se atoms are not bound to the surfactants. It is also found that the size-dependent behaviors of the distinct tetrahedral bond lengths $R^{(1)}$ and $R^{(2)}$ is consistent with those of wurtzite lattice parameters *c* and *a*, respectively. The structural distortion of the nanocrystals is explained as due to surface stress depending on the surface passivation and atomic relaxation related to the presence of stacking faults.

3.8 References

[1] A. N. Goldstein, C. M. Echer, and A. P. Alivisatos, Science **256**, 1425 (1992).

[2] J. N. Wickham, A. B. Herhold, and A. P. Alivisatos, Phys. Rev. Lett. **84**, 923 (2000).

[3] B. Gilbert, H. Zhang, F. Huang, J. F. Banfield, Y. Ren, D. Haskel, J. C. Lang, G. Srajer, A. Jürgensen, and G. A. Waychunas, J. Chem. Phys. **120**, 11785 (2004).

[4] P. Kluth, B. Johannessen, V. Giraud, A. Cheung, C. J. Glover, G. de M. Azevedo, G. J. Foran, and M. C. Ridgway, Appl. Phys. Lett. **85**, 3561 (2004).

[5] Y. Champion, F. Bernard, N. Millot, and P. Perriat, Appl. Phys. Lett. **86**, 231914 (2005).

[6] S. H. Tolbert and A. P. Alivisatos, J. Chem. Phys. **102**, 4642 (1995).

[7] R. W. Meulenberg, T. Jennings, and G. F. Strouse, Phys. Rev. B **70**, 235311 (2004).

[8] A. Marbeuf, M Barbe, A. Ramos, C. Levelut, and S. Wszolek, Acta Cryst. **B50**, 326 (1994).

[9] A. Guinier, *X-ray Diffraction in Crystals, Imperfect Crystals and Amorphous Bodies* (Freeman, San Francisco, 1963).

[10] C. B. Murray, D. J. Norris, and M. G. Bawendi, J. Am. Chem. Soc. **115**, 8706 (1993).

[11] M. G. Bawendi, A. R. Kortan, M. L. Steigerwald, and L. E. Brus, J. Chem. Phys. **91**, 7282 (1989).

[12] B. T. M. Willis and A. W. Pryor, *Thermal Vibrations in Crystallography* (Cambridge University Press, Cambridge, 1975).

[13] I.-K. Jeong, Th. Proffen, F. Mohiuddin-Jacobs, and S. J. L. Billinge, J. Phys. Chem. A **103**, 921 (1999).

[14] D. T. Cromer and J. B. Mann, Acta Crystallogr. Sect. A **24**, 321 (1968).

[15] JCPDS-International Centre for Diffraction Data (1998).

[16] A. W. Stevenson and Z. Barnea, Acta Cryst. **B40**, 530 (1984).

[17] C. Kumpf, R. B. Neder, F. Niederdraenk, P. Luczak, A. Stahl, M. Scheuermann, S. Joshi, S. K. Kulkarni, C. Barglik-Chory, C. Heske, and E. Umbach, J. Chem. Phys. **123**, 224707 (2005).

[18] A. C. Carter, C. E. Bouldin, K. M. Kemmer, M. I. Bell, J. C. Woicik, and S. A. Majetich, Phys. Rev. B **55**, 13822 (1997).

[19] M. Grundmann, O. Stier, and D. Bimberg, Phys. Rev. B **52**, 11969 (1995).

[20] C. Y. Yeh, Z. W. Lu, S. Froyen, and A. Zunger, Phys. Rev. B **46**, 10086 (1992).

[21] P. Perriat and J. -C. Niepce, High Temp. Chem. Processes **3**, 585 (1994).

[22] S. Banerjee, S. Jia, D. I. Kim, R. D. Robinson, J. W. Kysar, J. Bevk, and I. P. Herman, Nano Lett. **6**, 175 (2006).

[23] J. A. Majewski and P. Vogl, MRS Internet J. Nitride Semicond. Res. **3**, 21 (1998).

[24] P. Perriat, J. C. Niepce and G. Caboche, J. Therm. Anal. **41**, 635 (1994).

[25] V. A. Fedorov, V. A. Ganshin, and Yu. N. Korkishko, Phys. Status Solidi (A) **126**, K5 (1991).

[26] R. J. Bandaranayake, G. W. Wen, J. Y. Lin, H. X. Jiang, and C. M. Sorensen, Appl. Phys. Lett. **67**, 831 (1995).